Reynolds-Averaged Turbulence Model Assessment for a Highly Back-Pressured Isolator Flowfield

R. A. Baurle and T. F. Middleton
Hypersonic Airbreathing Propulsion Branch, NASA Langley Research Center
Hampton, Va 23681

L. G. Wilson
Analytical Mechanics Associates, Inc.,
Hampton, Va 23681

ABSTRACT

The use of computational fluid dynamics in scramjet engine component development is widespread in the existing literature. Unfortunately, the quantification of model-form uncertainties is rarely addressed with anything other than sensitivity studies, requiring that the computational results be intimately tied to and calibrated against existing test data. This practice must be replaced with a formal uncertainty quantification process for computational fluid dynamics to play an expanded role in the system design, development, and flight certification process. Due to ground test facility limitations, this expanded role is believed to be a requirement by some in the test and evaluation community if scramjet engines are to be given serious consideration as a viable propulsion device. An effort has been initiated at the NASA Langley Research Center to validate several turbulence closure models used for Reynolds-averaged simulations of scramjet isolator flows. The turbulence models considered were the Menter BSL, Menter SST, Wilcox 1998, Wilcox 2006, and the Gatski-Speziale explicit algebraic Reynolds stress models. The simulations were carried out using the VULCAN computational fluid dynamics package developed at the NASA Langley Research Center. A procedure to quantify the numerical errors was developed to account for discretization errors in the validation process. This procedure utilized the grid convergence index defined by Roache as a bounding estimate for the numerical error. The validation data was collected from a mechanically back-pressured constant area (1 × 2 inch) isolator model with an isolator entrance Mach number of 2.5. As expected, the model-form uncertainty was substantial for the shock-dominated, massively separated flowfield within the isolator as evidenced by a 6 duct height variation in shock train length depending on the turbulence model employed. Generally speaking, the turbulence models that did not include an explicit stress limiter more closely matched the measured surface pressures. This observation is somewhat surprising, given that stress-limiting models have generally been developed to better predict shock-separated flows. All of the models considered also failed to properly predict the shape and extent of the separated flow region caused by the shock boundary layer interactions. However, the best performing models were able to predict the isolator shock train length (an important metric for isolator operability margin) to within 1 isolator duct height.

[†] Approved for public release; distribution is unlimited.

INTRODUCTION

A dual-mode scramjet engine (see Fig. 1) is composed of four main components: inlet, isolator, combustor, and exit nozzle. The inlet captures the air mass for the engine and conditions (compresses) the flow for subsequent combustion. The role of the isolator is to separate the combustion effects (*i.e.* combustion-induced pressure rise) from the inlet, providing sufficient margin to prevent engine un-start. The combustor contains the fuel injection devices through which fuel is introduced and subsequently mixed with the incoming air allowing for combustion. Finally, the nozzle expands the resulting exhaust gases to produce thrust for the vehicle. At low hypersonic Mach numbers, the heat release associated with the combustion process can lead to (or at least approach) thermal choking of the engine flow, resulting in elevated pressure levels in the combustor. The adverse pressure gradient that forms under these conditions leads to the formation of a pre-combustion shock train within the isolator. This flow is characterized by regions of massive flow separation due to the adverse pressure gradient and the multiple shock/boundary layer interactions that result from this shock system. The isolator length required to contain the pressure rise induced by the combustion processes is of critical importance to the engine designer, since this drives the size (and weight) of the isolator section.

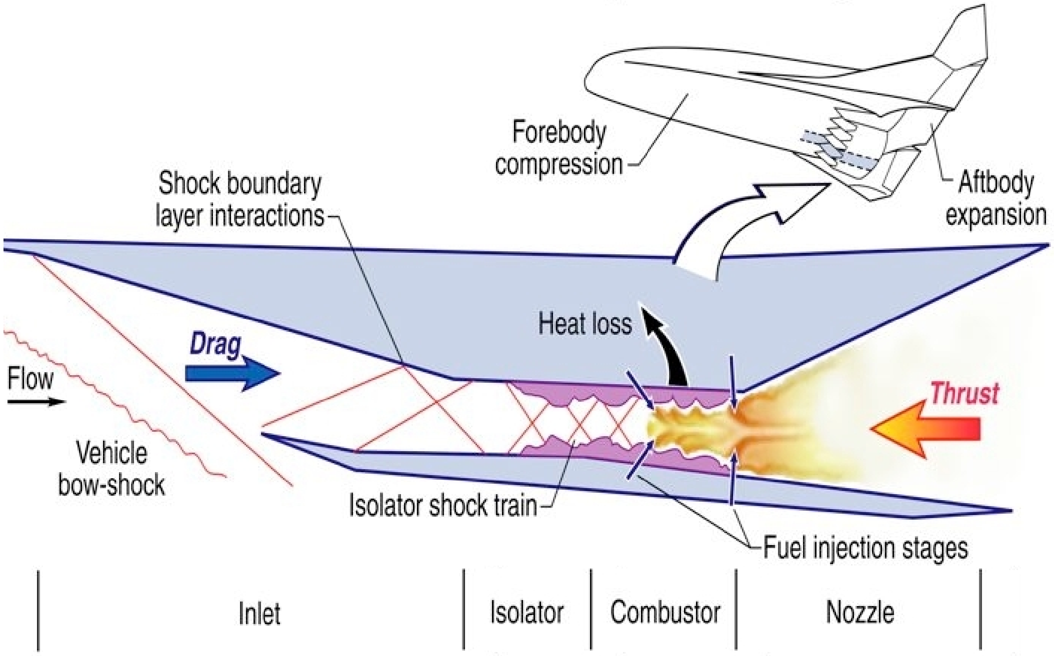

Figure 1: Dual-mode scramjet engine flowfield characteristics

Computational Fluid Dynamics (CFD) has been used extensively to fill critical gaps present in scramjet engine research and development. The heavy reliance on CFD is driven by several factors that include:

- difficulties with replicating hypersonic conditions in ground test facilities for sufficient periods of time
- obstacles with utilizing advanced diagnostics in the harsh scramjet flow environments
- lack of facilities large enough to test full-scale engines, other than possibly missile applications

Reynolds-Averaged Simulations (RAS) have been used almost exclusively to fill these gaps due to the enormous computational resources required to perform scale-resolved calculations such as Large Eddy Simulation (LES). The epistemic uncertainties (*i.e.* systematic uncertainties) associated with imperfect physical models used within a RAS framework are often found to dominate the overall uncertainty in simulations of scramjet flowpaths. [1, 2] If CFD is to be used as a predictive tool in the design and analysis of scramjet components, these model-form uncertainties must be well quantified. The quantification of these uncertainties will require that the models in question be validated for their intended purposes (*i.e.* for realistic geometries in representative flow environments). To date, while the use of CFD is prevalent, very few efforts have been undertaken that truly attempt to validate models for component level simulations. Instead, the current state-of-the-art relies heavily on the experience of the CFD practitioner to estimate the model-form uncertainty associated with their simulations through simple sensitivity studies. This practice will have to be replaced with a formal uncertainty quantification process if CFD is to play an expanded role in the Design Development Research and Engineering community, Development Test and Evaluation community, and ultimately certification for flight. This is especially true with hypersonic air-breathing propulsion systems due to the environment, scale, and duration limitations of ground test facilities. The work described here represents a step toward enabling a process for quantifying model-form uncertainties for the isolator component of a dual-mode scramjet engine. In particular, the purpose of this effort is to document the initial stages of a formal model validation process underway at the NASA Langley Research Center for the flow physics present in scramjet isolators.

FACILITY DESCRIPTION

The Isolator Dynamics Research Laboratory (IDRL) has recently been brought on-line by the Hypersonic Airbreathing Propulsion Branch at the NASA Langley Research Center. A photograph and schematic of the facility hardware are given in Fig. 2. The flowpath is mounted vertically with facility flow directed from bottom to top. A unique aspect of this facility is the ability to translate and/or rotate the rig during facility operation. This capability was desired to simplify the application of advanced laser-based diagnostics for flowfield interrogation. The ability to move the test apparatus allows the diagnostic equipment to be set-up and aligned only once, so that the diagnostic components never have to be relocated. Air is supplied via 4 flexible hoses to a settling chamber that houses a honeycomb flow straightener to remove swirl and reduce freestream turbulence levels. The settling chamber connects to a planar Mach 2.5 nozzle that was designed using an inviscid method-of-characteristics code coupled with a two-dimensional full Navier-Stokes solver. The 24-inch isolator test section has a height (h) of 1-inch and a width (w) of 2-inches, and is constructed through any combination of glass and metallic side walls. Hence, both wall measurements and laser-based in-stream measurements can be obtained simultaneously. The metal walls were installed for this effort, allowing for a total of 213 static pressure measurements in the arrangement shown in Fig. 3. The flow exits the isolator test section and enters a 15-inch long cylindrical expansion section that is machined with a 45° chamfer on the downstream end to mate with a back-pressure plug. The back-pressure plug is mounted in the spool section to a linear actuator that positions the plug with a precision of 1/1000 of an inch. The back-pressure plug simulates the thermal choking effect caused by combustion in a dual-mode scramjet engine, providing a means of creating the back pressured isolator flowfield of interest. A detailed discussion of the facility is given in Ref. 3.

COMPUTATIONAL DESCRIPTION

The computational domain considered spans the region from the facility nozzle plenum to the end of the 24-inch isolator duct. The geometrical symmetry present in this flowpath, and the fact that only steady-state simulations are to be performed, permitted the consideration of only one quarter of the facility flowpath as shown in Fig. 4. A structured grid with a total of 85,196,800 cells was created for the simulations with 18,636,800 cells placed in the nozzle block ($560 \times 160 \times 208$), and the remaining 66,560,000 cells ($2000 \times 160 \times 208$) in the isolator duct. Two coarser grids (10,649,600 and 1,331,200 cells) were obtained from this parent grid via a factor of 2 coarsening in each coordinate direction to allow for a formal assessment of the numerical errors associated with the simulations. The grid points were clustered near the walls such

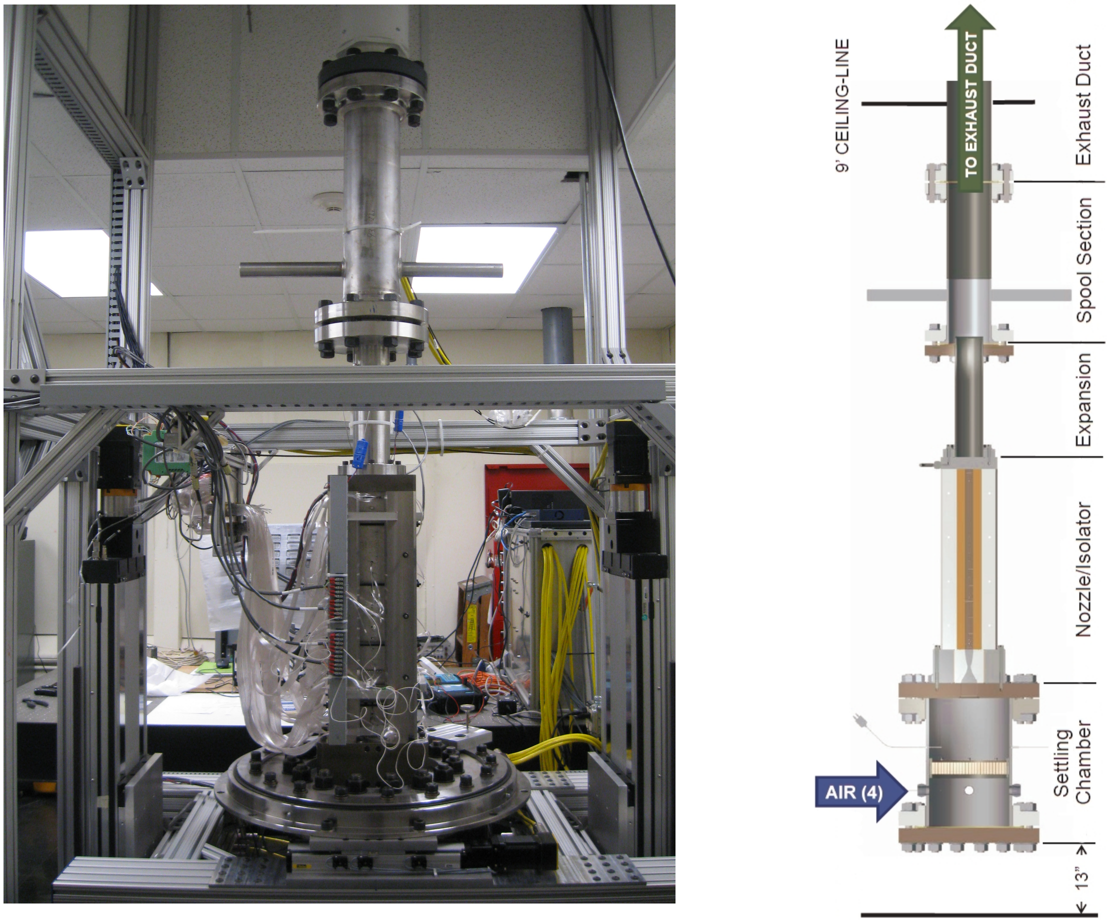

Figure 2: Photograph (left) and schematic (right) of the Isolator Dynamics Research Laboratory hardware

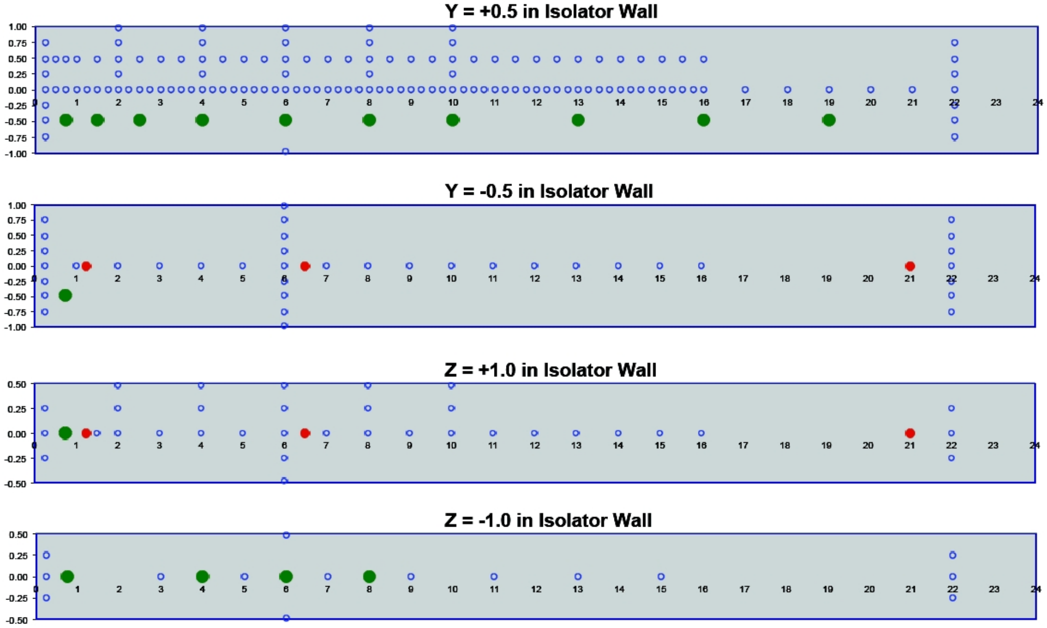

Figure 3: Instrumentation layout for the metallic isolator side walls: static pressure ports (blue), thermocouples (red), high frequency pressure ports (green)

that the maximum y^+ value at any cell center adjacent to the surface was no greater than 1 (approximately) for the coarsest grid considered. The grid was also clustered in the streamwise direction at the nozzle throat (Δx = 0.0025 h) with the spacing gradually increased to 0.01 h at the nozzle exit. The streamwise spacing was held fixed at 0.01 h for the front half of the isolator to resolve the region where the shock train was expected to reside, and was stretched in the second half of the isolator to a value of 0.025 h at the isolator exit. The maximum grid spacing in the vertical (y) and spanwise (z) directions was 0.01 h (adjacent to the planes of symmetry). The entire grid was split up into a total of 1280 grid blocks which yielded good (95% or better) load balance statistics for up to 438 processors.

All computational results were obtained using the VULCAN (Viscous Upwind aLgorithm for Complex flow ANalysis) Navier-Stokes code. [4] This CFD package is developed and maintained by researchers in the Hypersonic Airbreathing Propulsion Branch at the NASA Langley Research Center, and the development of this software has predominantly been driven by the needs of the scramjet community. The CFD data obtained in this effort were acquired by integrating the Reynolds-Averaged Navier-Stokes equations until steady-state conditions were achieved. All of the solutions were advanced in pseudo-time via an incomplete LU factorization scheme (with planar relaxation) using a Courant-Friedrichs-Lewy (CFL) number of 100. The inviscid fluxes were evaluated using the Low-Diffusion Flux Splitting Scheme of Edwards, [5] with cell interface variable reconstruction achieved via the κ=1/3 Monotone Upstream-centered Scheme for Conservation Laws. The Koren flux limiter [6] was utilized to avoid spurious oscillations during this reconstruction process. The viscous fluxes were evaluated using 2^{nd}-order accurate central differences with the viscosity of air computed from the polynomial fit of McBride. [7, 8] The molecular and turbulent Prandtl numbers were set to 0.72 and 0.9, respectively. An adiabatic no-slip condition was applied at all solid surfaces. The subsonic nozzle plenum inflow condition was specified based on the measured plenum pressure and temperature, with Mach number extrapolated from the interior. Finally, all properties were extrapolated at the subsonic exit of the isolator with the exception of the static pressure. The static pressure was set to the value obtained by averaging the 20 surface pressure measurements taken around the periphery of the isolator duct at the x=22 h station. This station was highly instrumented with pressure taps for the specific purpose of providing a well characterized outflow boundary condition.

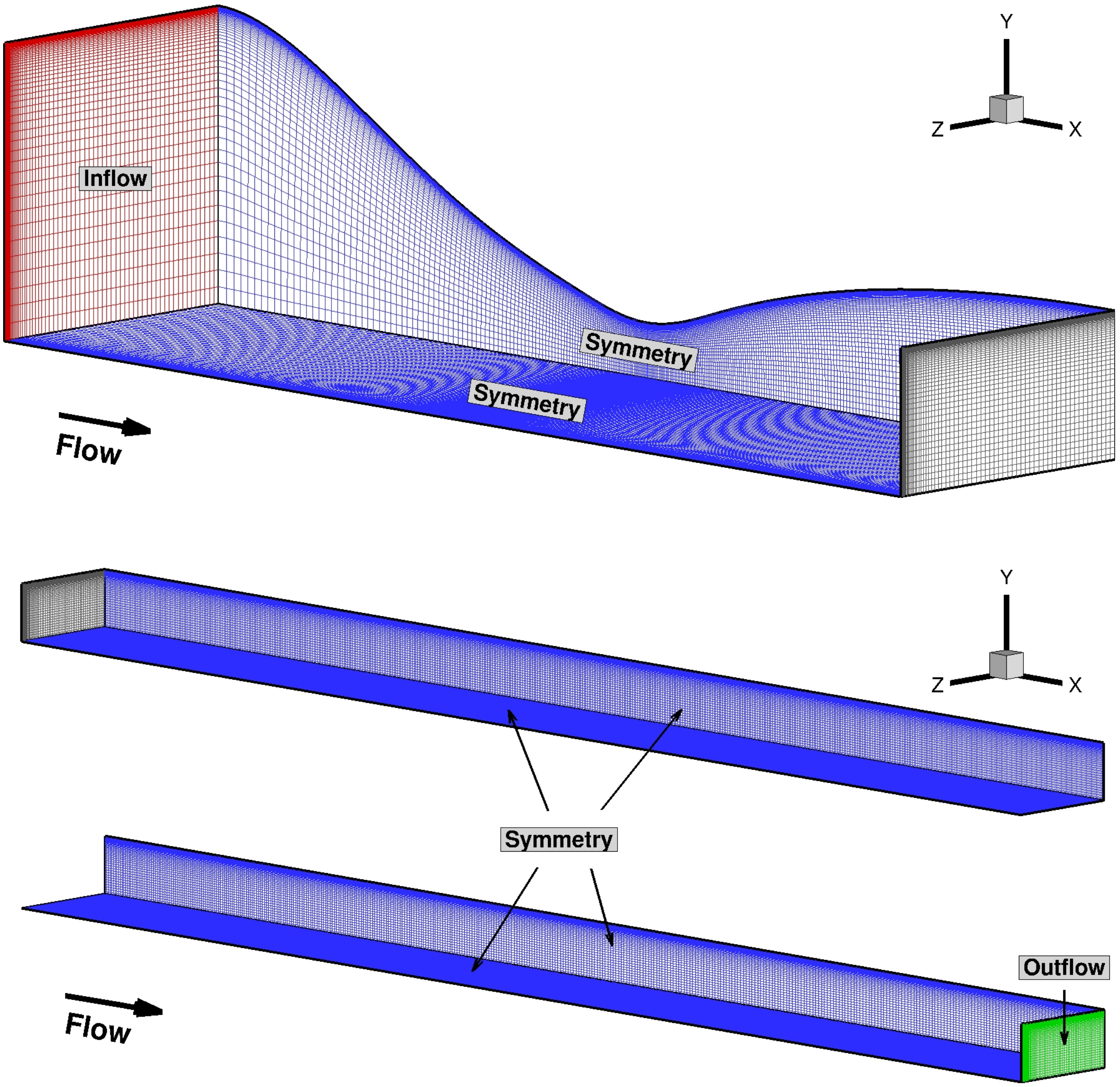

Figure 4: Grid created for the nozzle/isolator assembly (every other point removed for clarity): nozzle section (top), first half of isolator section (middle), second half of isolator section (bottom)

Five different turbulence models were assessed in this effort: Menter BSL,[9] Menter SST,[9] Wilcox 1998,[10] Wilcox 2006,[11] and the Gatski-Speziale Explicit Algebraic Stress Model (EASM).[12] The implementation of these models is precisely as described in the references cited above, with the following (potential) exceptions:

- The "exact" production term in the transport equation for the turbulence kinetic energy ($i.e.\ \tau_{ij}\frac{\partial u_i}{\partial x_j}$) was consistently utilized.
- The production of turbulence kinetic energy (k) was limited to be no more than 10 times the destruction of k to discourage spurious production of turbulence across shock waves.
- The surface boundary condition for the specific dissipation rate (ω) was set as suggested by Menter[9] to be 10 times the derived asymptotic value.
- The modification to the destruction term coefficient for the ω equation in the Wilcox models that addresses the "round jet / plane jet anomaly" was omitted due to undesirable (and unintended) effects noted in the shock separated regions.

It is also worth noting that a variety of sensitivity studies were performed to address the impact of modeling decisions other than the choice of turbulence model. These simulations were performed to ensure that any variability in the simulation results of interest were small relative to variations expected as the turbulence models are varied. Modeling sensitivities that were considered include:

- choice of turbulent Prandtl number (varied between 0.7 and 1.1)
- choice of model for the turbulence production term (exact or approximate formulation based on the vorticity magnitude)
- choice of limiting value placed on the production to destruction ratio for k (limited by 10 or unlimited)
- choice of viscous constitutive relation (Sutherland law or McBride polynomial)

Although not detailed in this document, the solution variability associated with these sensitivities were small relative to variations noted when changing the turbulence model; confirming that the turbulence model closure is the dominant source of epistemic uncertainty for this flowfield class. Finally, additional simulations were performed to check for hysteresis since it is known that flows with massive separation can be sensitive to how the separations develop during the process of converging to a steady-state. In particular, simulations were performed using an initial condition based on an existing converged solution (obtained from the use of a different turbulence model) to ensure that the results matched those obtained by the default initialization procedure. While the authors do not definitively claim that the solutions obtained are not in some way influenced by how the flowfields were initialized, these checks at least ensured that the solutions obtained were achievable via more than one numerical solution path.

RESULTS AND DISCUSSION

The IDRL facility was designed from its inception with CFD validation in mind. Toward this end, both Experimental Fluid Dynamics (EFD) and CFD researchers were involved in all stages of the design process. This collaboration was crucial to ensure that all data requirements (as defined by the CFD team) and measurement capabilities (as defined by the EFD team) were communicated. This communication led to the determination of the diagnostic approaches to employ, and the hierarchy of measurements required, to maximize the value of the experimental data. Additional highlights from this collaboration are listed below (the details of which can be found in Ref. 13):

- CFD simulations were conducted to define facility requirements, including:
  - sensitivity studies to determine the control authority (precision) required for the back-pressure plug
  - sensitivity studies to determine the control authority requirements for the facility supply pressure
  - sensitivity studies to determine the influence of supply temperature (and surface temperature) to determine whether a temperature control system should be considered
  - sensitivity studies to determine the influence of facility supply air turbulence levels
- Instrumentation layout was defined (to a large extent) by the CFD team with particular emphasis placed on measurements required to specify and/or assess boundary conditions.
- CFD simulations were performed to determine the ramification of slot openings present in the specially designed isolator side walls required by some of the advanced laser-based diagnostics (not present in this study).

Solution Verification

The initial step of any validation effort requires an assessment of numerical errors. Numerical errors are denoted here as spatial discretization errors and iterative convergence errors. Temporal discretization errors are of no consequence for this study since only steady-state simulations are considered. The most compelling proof of iterative convergence is the situation where the residual norms have been reduced to machine accuracy. Unfortunately, this situation is rarely realized in practice, particularly when simulating complex flows with shock waves and regions of massive flow separation. Alternatively, the L_2 norm of the residual is monitored until it levels out about some acceptably low value. In addition, the variability of integral properties of interest such as mass flow rates and surfaces loads are checked to offer further assurance that an adequate level of convergence has been achieved. In general, the following iterative convergence statements were satisfied for each simulation discussed in this effort (also see Fig. 5 for a typical convergence history):

- The value of the residual L_2 norm was reduced by at least 5 orders of magnitude.
- The integrated surface load time histories were unchanged (to at least 5 significant digits) over the last 5000 iteration cycles.
- The integrated mass flow rate was constant at every streamwise grid plane to 4 significant digits.

The Grid Convergence Index (GCI) [14] was used to quantify the spatial discretization (*i.e.* grid convergence) error. The GCI is a grid convergence estimator derived from the generalized Richardson Extrapolation formula, and can be written as follows:

$$\mathrm{GCI} = F_s \frac{|\epsilon|}{r^p - 1} \tag{1}$$

In this expression, ϵ is the difference of some functional "f" evaluated using two different grid resolutions with refinement ratio r, *i.e.*

$$\epsilon = f_2 - f_1 \tag{2}$$

and p is either the observed order of accuracy of the numerical scheme or taken to be 2 (*i.e.* 2^{nd}-order). Finally, F_s is a "factor of safety" with recommended values taken to be either 3 (if the observed order of accuracy is assumed to be the theoretical value) or 1.25 (if the observed order of accuracy has been rigorously determined). It should be emphasized that the GCI, while based on Richardson Extrapolation, is not meant to be a "best estimate" of the numerical error. Instead, the intent is to provide a reasonable bound on the discretization error.

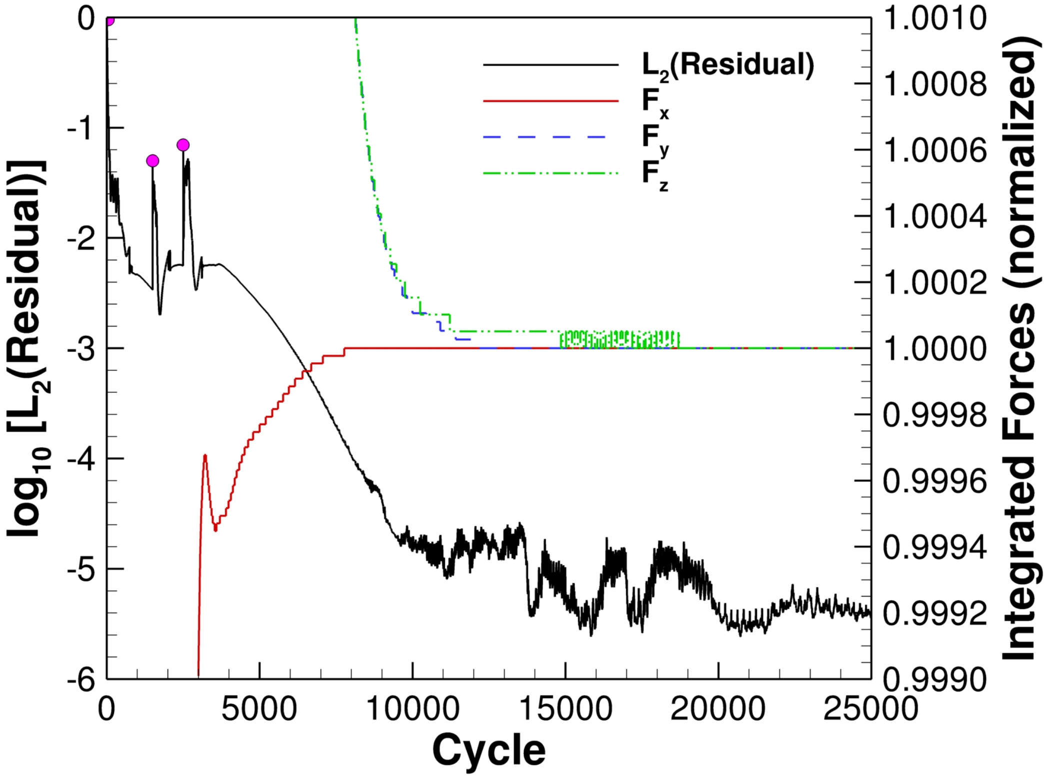

Figure 5: Iterative convergence measures (circles show start of coarse, medium, and fine grid sequences)

The observed order of accuracy was extracted from the isolator simulations performed in this effort. A minimum of three grids are required to facilitate the extraction of the observed order of accuracy via the following expression:

$$p = \ln\left(\frac{f_3 - f_2}{f_2 - f_1}\right) \;/\; \ln(r) \tag{3}$$

The coarse grids were obtained by systematically removing every other point from the grid that was generated, resulting in a refinement (or coarsening) ratio of r=2. The subscript of each functional denotes the grid level with “1” representing the finest grid and “3” representing the coarsest. Note that this expression implicitly assumes that solutions obtained from each grid level are within the asymptotic range of convergence. There is no way to formally prove that each grid level satisfies this constraint (without adding yet another grid level). However, the coarsest grid was designed to maintain a y^+ value near unity (or less) adjacent to each solid surface, and was judged to offer adequate resolution based on past experience with performing simulations of this type. Moreover, sanity checks were performed using a variety of functionals to check that the order of accuracy extracted was consistent between functionals of a given class.

The conditions chosen to assess the observed order of accuracy were based on flow conditions that result in a pressure ratio across the isolator shock train that is approximately 80% of the normal shock value based on the approach flow Mach number. This condition represents a realistic operability limit that dual-mode scramjets are often designed to, and is a close match to the conditions that will be utilized for the validation exercises. The precise conditions chosen are given in Table 1. The turbulence model selected for this exercise was the Menter BSL model.

The isolator flowfield obtained from these flow conditions is presented in Fig. 6. The global isolator shock train structure (visualized by the velocity divergence) consists of leading oblique shock waves followed by alternating expansions and quasi-normal shocks. The top image shows static pressure contours superimposed on an iso-surface of the total pressure (P_o=300 kPa). This image provides a visual of the core flow

Table 1: Facility flow conditions chosen for order of accuracy assessment

Nozzle Plenum Pressure [kPa]	861.85
Nozzle Plenum Temperature [K]	298.15
Nozzle Exit Mach Number	2.5 *
Nozzle Exit Pressure [kPa]	50.44 *
Isolator Exit Pressure [kPa]	296.50

* Nominal value computed from isentropic relationships

displacement caused by the interactions between the shock waves and the turbulent boundary layer that engulfs the isolator walls. The area blockage caused by the separated flow in the corners is a dominant feature that dictates (to a large extent) the shock train flow structure. The Mach number contours show a boundary layer structure on the vertical side walls that is notably thicker near the center of the side wall. This feature is a result of the expansion processes in the facility nozzle, and makes this particular boundary layer more susceptible to large-scale flow separation. Mach disks are also seen in the center of the duct, and while it is difficult to visualize in this image, the interaction of the leading oblique shock wave and the Mach disk results in the formation of a shear layer. The flow in the isolator initially separates in the corners of the duct where the shear forces are weakest. This separation results in a conical shock that spreads diagonally across the isolator; diverting the flow toward the center of the duct. The high pressure that is produced in the corners also drives the the boundary layer fluid away from the corners along the adjacent walls. The side walls (z=constant vertical surfaces) are half the width of the top and bottom walls (y=constant spanwise surfaces), so the effect of the adverse pressure gradient formed in the corners influences the center of the vertical walls more quickly than their spanwise counterparts. The additional width offered by the spanwise surfaces allows sufficient space for a second separation region to form at the z=0 centerplane of the duct. This separation bubble forms a strong oblique shock followed by a strong expansion as this separation zone re-attaches to the surface. The resulting flow remains attached along the isolator centerplane even after further shock reflections downstream. The separation zones that originate in the corners, however, gradually extend across the side walls and persist for several duct heights further downstream. Moreover, the increased turbulence levels present in these separated flow zones do not dissipate as the flow progresses downstream. The eventual result of this unbalanced production of turbulence is a very large “effective” viscosity across the entire width of the duct that is 20,000 times larger than the local fluid viscosity. The net effect is a flowfield that exits the isolator with properties representative of a Reynolds number that is 4 orders of magnitude lower than the flow entering the isolator. This behavior is the mechanism that allows a Reynolds-averaged simulation to produce a steady-state solution for this flow.

A total of 5 functionals (representing 2 functional classes) were extracted from this flowfield to perform the order of accuracy assessment. The surface shear (skin friction) at the nozzle exit defined one functional class of interest. This parameter provides a measure of how resistant the approach flow boundary layer is to flow separation. The wall shear along the center of both the vertical and spanwise surfaces was extracted and used to compute the order of accuracy for this functional class. The second functional class considered involved measures of isolator shock strength. Local measures of shock properties were avoided since the theory behind Richardson Extrapolation (which is based on a Taylor series expansion) breaks down for properties that are discontinuous. Instead, the integrated isolator surface force components and incipient shock locations were considered for the order of accuracy assessment within this class.

The results of the order of accuracy assessment are given in Table 2, showing that the observed order of accuracy is only 1^{st}-order even though a nominally 2^{nd}-order spatial scheme was utilized. This behavior, while troubling, can be explained by noting that a non-linear TVD (Total Variation Diminishing) flux limiter was invoked to capture the anticipated strong shocks with minimal dispersion. The TVD property of these limiters forces the numerical scheme to become locally 1^{st}-order accurate whenever a flow property extrema is encountered. As pointed out by Roache, [14] it is not uncommon for errors introduced by localized 1^{st}-order treatments to propagate to other areas of the flowfield. This is particularly true for systems of equations

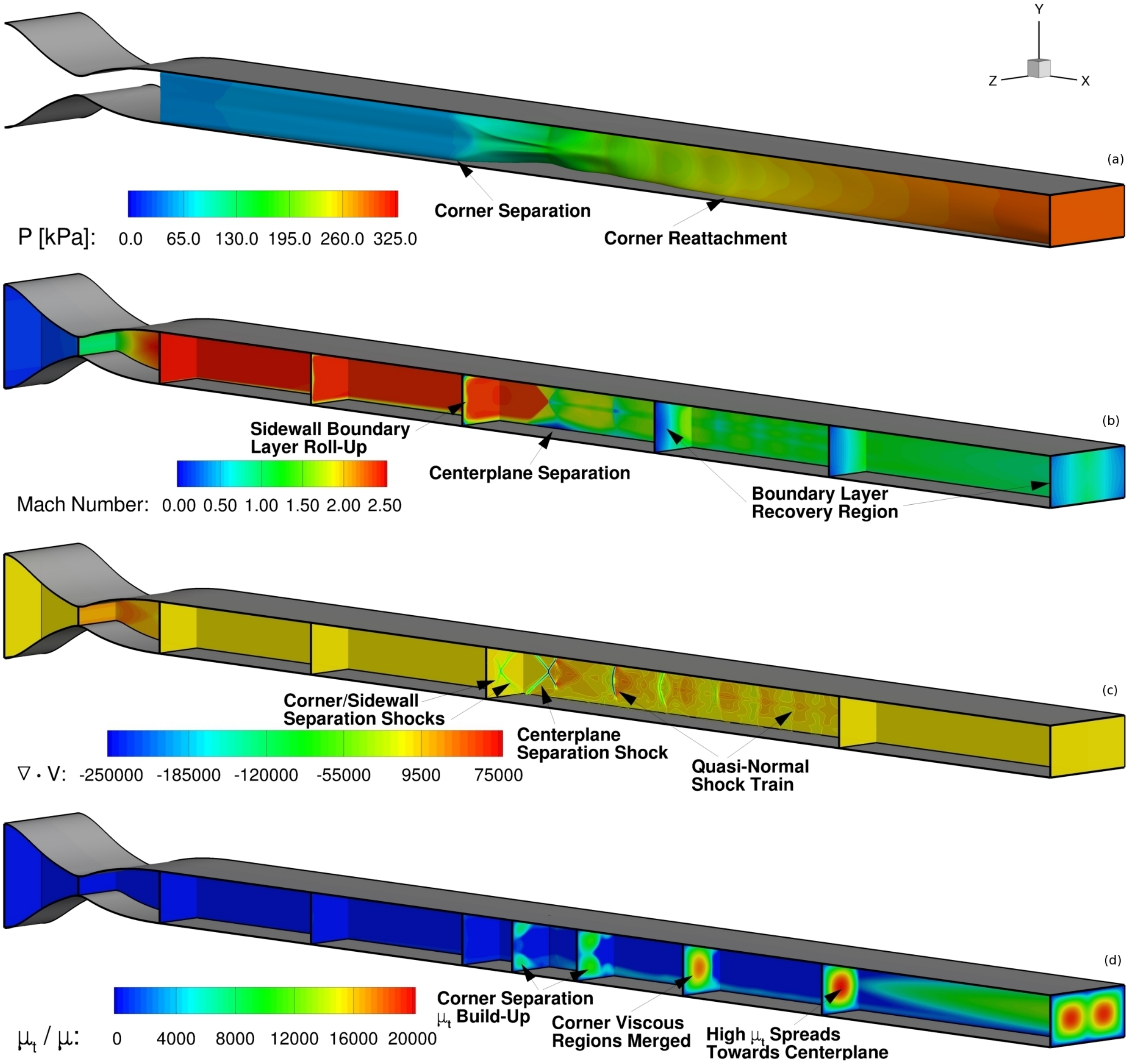

Figure 6: Isolator flowfield characteristics: (a) total pressure iso-surface colored by static pressure contours, (b) Mach number contours (c) velocity divergence contours, (d) turbulent to molecular viscosity ratio contours

where more than one family of characteristics are present for information propagation. It should also be emphasized that although the order of accuracy assessment shows the rate of grid convergence to be 1^{st}-order, the solution accuracy is considerably higher than what would have been obtained using a globally 1^{st}-order algorithm on the same grid. In other words, the extracted order of accuracy simply provides a statement on the rate of grid convergence, and in isolation should not be used to judge solution accuracy.

Table 2: Extracted order of accuracy for each functional

Functional	Fine Grid	Medium Grid	Coarse Grid	Accuracy Order
Nozzle Exit C_f (spanwise centerline)	1.0956×10^{-4}	1.0831×10^{-4}	1.0572×10^{-4}	1.05
Nozzle Exit C_f (vertical centerline)	1.0042×10^{-4}	9.9776×10^{-5}	9.8142×10^{-5}	1.33
Isolator Surface F_x [N]	6.1311	6.0661	5.9228	1.14
Isolator Surface F_y [N]	2735.4	2698.2	2625.3	0.97
Isolator Surface F_z [N]	1368.2	1349.6	1312.9	0.98
Spanwise centerline shock location *	8.8734	9.1631	9.7621	1.05
Vertical centerline shock location *	8.2825	8.5850	9.2228	1.08
Corner shock location *	7.7942	8.0967	8.7417	1.09

* Shock location defined as the distance from the nozzle exit (x/h) where the shock-induced pressure rise is 2.5 psi (17.237 kPa)

Having established the order of accuracy of the simulations, the following recipe was utilized to quantify (in the form of an error band) the numerical error associated with the simulations for all subsequent validation exercises. First, it was assumed that the order of accuracy extracted from the simulations described above is applicable to the simulations performed for each of the turbulence models being validated. This was deemed to be a reasonable assumption given the fact that the turbulence models considered in this effort (with the exception of the EASM formulation) are functionally quite similar. Moreover, given that the observed order of accuracy was only 1^{st}-order, the use of p=1 in the expression for the GCI (see Eq. 1) provides a conservative estimate of the numerical error. The order of accuracy would only increase (if it changed at all) if this process were to be repeated for each turbulence model, so in the spirit of attempting to bound the error (rather than get a best estimate of it), the value of p was set to 1.0 for all GCI evaluations. This approach allows the use of only the medium and coarse grids in all remaining simulations for validation purposes; reducing the computational costs by at least an order of magnitude. Given the observed order of accuracy and the relationship for the GCI, an error band for the shock train position is computed for inclusion in the plots as an error bar. The error bar is one-sided, rather than symmetrically placed about the computed data point, because as the grid is resolved the variation of a given functional is monotonic (provided that each grid is within the asymptotic convergence range).

An illustration of this strategy for reporting the numerical error is given in Fig. 7. In this example, the numerical error “bound” for the spanwise symmetry plane surface shock position has been quantified using the GCI for this functional given the observed order of accuracy (p=1) and the coarse and medium grid shock position values taken from Table 2. The spanwise centerline surface pressure trace extracted from the fine grid solution has been included as a surrogate “truth” value. The error bars based on the GCI (computed for both the medium grid and coarse grid solutions) clearly bracket every data point of the fine grid simulation. While this does not prove that the numerical error has been rigorously bounded, it does provide some confidence that the approach is yielding a reasonable quantified bound of the numerical error. As a final note, Fig. 8 compares all three pressure traces, with the coarse and medium grid results translated to provide a best-fit to the fine grid data. The close match after translation supports the choice of using shock position as an error indicator rather than the discrete surface pressure values which vary discontinuously across shocks. The fact that the numerical error primarily resulted in a delayed initiation of the shock train, and did not alter the detailed shock structure to any meaningful degree, allowed the use of a scalar GCI value (shock position) rather than a more complicated approach based on an array of GCI values computed from spatially varying properties.

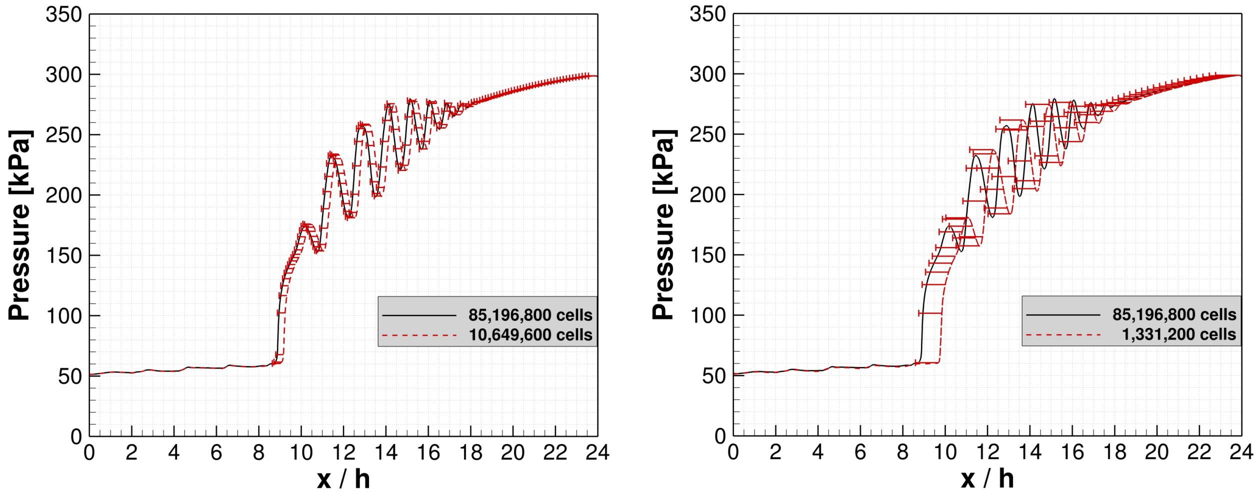

Figure 7: Comparison of fine grid wall pressure (spanwise centerline) with the medium grid results (left) and the coarse grid results (right); error bars represent the GCI estimated error bound

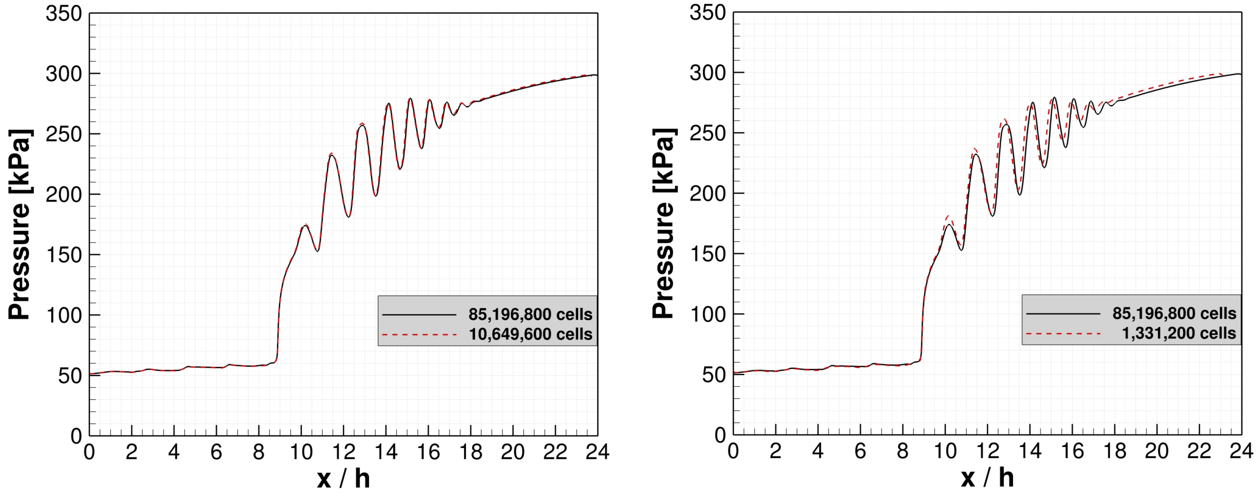

Figure 8: Comparison of fine grid wall pressure (spanwise centerline) with the translated medium grid results (left) and the translated coarse grid results (right)

Model Validation

The conditions of interest for the validation exercises are isolator conditions that result in a pressure ratio across the isolator shock train that approaches the operability bound of typical dual-mode scramjets. The IDRL isolator shock train length (L_{iso}) plotted as a percentage of the normal shock pressure ratio (based on the nominal isolator entrance Mach number of 2.5) is given in Fig. 9. The shock train length is defined as the distance from the location of the incipient shock-induced surface pressure rise to the exit of the isolator. This plot shows that the ability of an isolator to hold a given pressure ratio diminishes rapidly as the normal shock pressure ratio is approached. For the isolator conditions considered here, a 9% increase in the back pressure from 82.25% to 89.82% of the normal shock pressure rise changes L_{iso} by 8.6 x/h (or 35% of the available isolator length). The sensitivity of the shock position to the back pressure value in this regime is clearly a challenge for any simulation effort to accurately predict. This sensitivity also explains why dual-mode scramjets have historically been designed to limit the total combustor-induced pressure rise during low-speed operation to approximately 80% of the normal shock value based on the isolator approach flow Mach number.

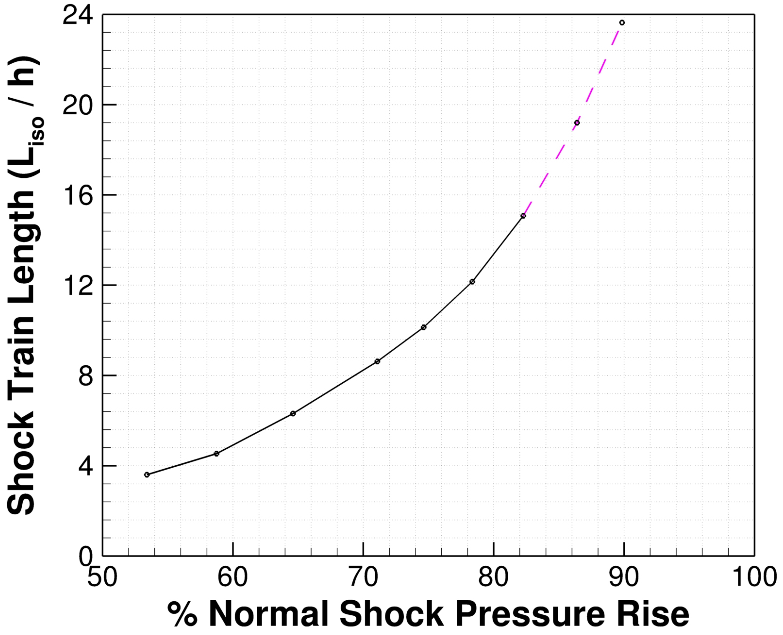

Figure 9: Isolator shock train length as a function of the normal shock pressure rise for a Mach 2.5 flow (dashed portion of the line represents an operability range beyond that of current designs)

The facility isolator conditions (with and without back pressure) considered for this validation exercise are given in Table 3. The measured conditions in this table, and the measured surface pressures in the plots that follow, are an ensemble average of measurements taken over an approximate 5 second test interval. The values in parenthesis represent the rms deviation in the measured values relative to the mean value obtained over the 5 second averaging interval. The IDRL facility has only very recently been brought on-line, and the uncertainty quantification process for the measurements has not been completed. As a result, only the measurement deviation rms over the test window is being reported at this time.

A comparison of surface pressure obtained from the medium grid with measurements for the fully supersonic (no applied back pressure) conditions is shown in Fig. 10. The simulated results shown are only those obtained with the Menter BSL turbulence model, since all of the turbulence models considered in this effort predict essentially the same surface pressure distribution when a back pressure is not applied. Two distinct observations are immediately apparent when comparing the simulations to the measured values. The first observation is that the residual wave structure exiting the nozzle is significantly stronger than what has

Table 3: Facility flow conditions selected for model validation

Facility Condition	Fully Supersonic	Back Pressured
Nozzle Plenum Pressure [kPa]	860.30 (0.013)	845.29 (0.025)
Nozzle Plenum Temperature [K]	297.00 (0.018)	292.91 (0.023)
Nozzle Exit Mach Number	2.5 *	2.5 *
Nozzle Exit Pressure [kPa]	50.35 *	49.47 *
Isolator Exit Pressure [kPa]	N/A	304.51 (0.097)

[*] Nominal value computed from isentropic relationships

been predicted. This result was expected to some extent, since there are known discrepancies between the as-designed (used for the simulations) versus the as-built nozzle geometry. The discrepancies are within the fabrication tolerances of the nozzle, but the team has not yet had the opportunity to address the impact of these geometrical differences. This will be a focal point in the next stage of this research effort. The more troubling observation is the systematic under-prediction of pressure throughout the entire length of the isolator. The two most obvious explanations for this particular disagreement are either a mismatch in the nozzle exit to throat area ratio or some sort of instrumentation problem. A careful examination of the nozzle assembly has ruled out the nozzle area ratio as a potential culprit. However, a comparison of the measured mass flow rate through the facility (via a Venturi flow meter) with the value obtained from choked flow relationships (given the facility plenum conditions and the nozzle throat area) revealed a discrepancy of approximately 3.3%. The measured mass flow rate was higher than the value obtained from the choked flow equations with a unity discharge coefficient, which clearly points to some issue with the instrumentation. Upon further examination, a problem with the facility plenum pressure measurement was uncovered, and further facility shake-down activities are underway to determine if the resolution of this problem eliminates the discrepancy with the Venturi flow rate measurement.

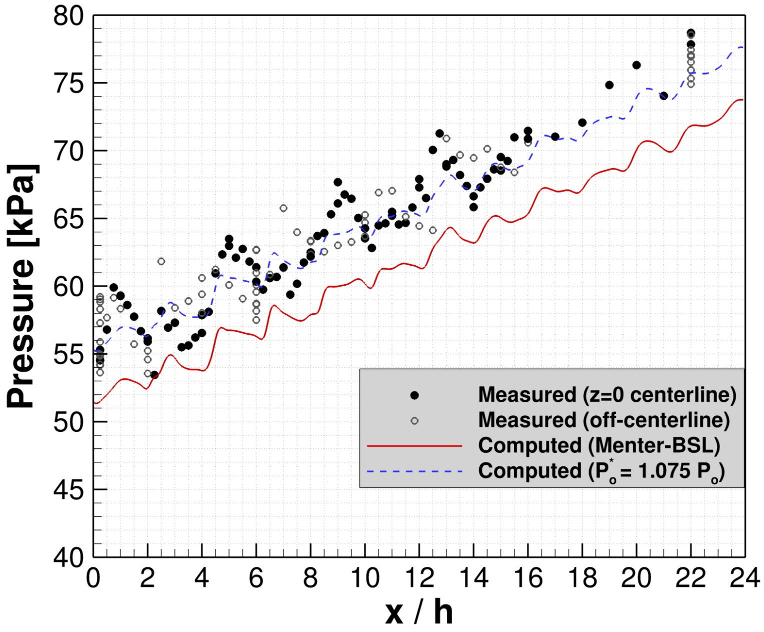

Figure 10: Comparison of measured wall pressure with computed results (medium grid) obtained for conditions without an imposed back pressure

Unfortunately the 3.3% discrepancy between measured and deduced flow rate, while in the right direction relative to the simulations, accounts for only about half of the difference between the simulated and measured wall pressure values. Fig. 10 shows something closer to a 7.5% increase in nozzle exit pressure is required to match the measured pressure levels in the isolator. As noted in Fig. 9, the shock train location is highly sensitive to the precise pressure rise across the shock train. Since the simulations use the measured back pressure as an outflow boundary condition, it is critical that the static pressure entering the isolator also be matched. Given that an issue was uncovered with the plenum pressure measurement, which is a measured value used as an inflow boundary condition, the decision was made to increase the plenum pressures given in Table 3 by 7.5% for the simulations. There are other boundary condition modifications that could have been made to match the overall pressure rise through the isolator, so an additional simulation was performed to assess this sensitivity. The additional simulation involved reducing the back pressure by 7.5%, while keeping the nozzle plenum pressure at the measured value. The difference in the normalized wall pressure distributions from each simulation is illustrated in Fig. 11. This difference, due solely to the slight disparity in Reynolds number, is smaller than the quantified numerical error, suggesting that the detailed method used to match the simulated conditions in to and out of the isolator is of little consequence. However, until the root cause of the discrepancy between measured and computed nozzle exit conditions is understood, the validation exercise will be incomplete. Hence, comparisons with the measured pressures that follow in the remainder of this paper should be regarded as preliminary results.

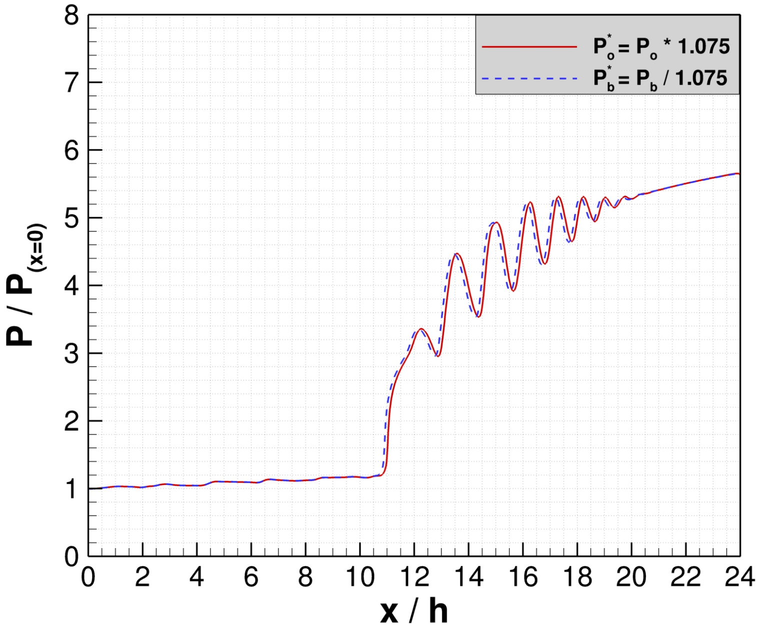

Figure 11: Normalized wall pressure distributions obtained via alternative boundary conditions that match the measured pressure rise

A comparison of the back pressured results obtained using the modified plenum pressure for each turbulence model are shown in Fig. 12. The computed results shown are those obtained from simulations that used the medium grid. The images on the left compare the pressure along the z=0 centerline of the top and bottom walls, while the images on the right compare pressure values along the y=0 centerline of the side walls. The error bars associated with the CFD results represent the numerical discretization error bound for shock position based on the approach described in the solution verification section. Overall, there is at least a 6 duct height variation in shock position depending on the turbulence model employed, so clearly the model-form uncertainty is significant. Some general observations drawn from these comparisons are listed below:

- The measured pressure distribution along the spanwise centerline (z=0) shows a monotonic rise, while the simulations do not.

- The computed side wall y=0 centerline pressure distributions display a monotonic rise (or at least nearly monotonic) which is consistent with the measurements.
- The two turbulence models that have an explicit stress limiter (Menter SST and Wilcox 2006) are the worst performers for this shock-dominated massively separated flow. The stress limited models also show opposite trends with respect to shock train position.
- To within the discretization error uncertainty, the remaining turbulence models predict a shock train length that is within 1 duct height of the measured value.

These observations are discussed in further detail in the paragraphs that follow.

Perhaps the most noticeable difference between the predicted and measured surface pressure distributions is the fact that the measured pressure distribution along the z=0 centerline shows a monotonic rise, while the computed distribution does not. A popular explanation for this behavior [2] is the observation that highly back-pressured isolator flowfields often exhibit large scale unsteadiness with shock train motions that can alter the L_{iso} at any given instance in time by several duct heights. Hence, the measured static surface pressure through the shock train actually represents some effective pressure gradient that results from the unsteady movement of the shock system. This is contrasted with a steady-state simulation where the shock system is fixed in time with no smoothing of the pressure rise due to unsteady shock motions. However, one can always ensemble average (in time) an unsteady system with shock waves to obtain a time-averaged state, and the resulting state will contain a stationary shock system. Hence, a less literal interpretation of this phenomenon revolves around what can reasonably be expected from a single point turbulence closure approximation. The closure models developed for Reynolds-averaged simulations are almost exclusively derived for attached shear-dominated flows. The ability of these models to accurately model the detailed effects caused by multiple unsteady shock waves interacting with an attached approach boundary layer is certainly questionable. In other words, the reason that the pressure rise is not monotonic may simply be a result of the fact that the shape and size of the recirculation zones are not accurately predicted by the models. Examples of efforts that attempt to model the complex effects of shock unsteadiness on Reynolds-averaged closure models are described in Refs. 15 and 16.

To illustrate the impact of the separated flow structure on the surface pressure, a simulation was performed using a modified IDRL isolator geometry where the width was increased from 2-inches to 4-inches (resulting in a cross-sectional aspect ratio of 4 instead of 2). The reasoning behind considering this geometry is based on this author's observation that steady-state Reynolds-averaged simulations tend to exaggerate the three-dimensional surface pressure features in the shock separated flow portion of the isolator. By increasing the aspect ratio of the isolator, the three-dimensional corner and side-wall effects are expected to be less dominant. A comparison of the surface pressure along the z=0 centerline for both isolator geometries is given in Fig. 13. Both of these simulations utilized the Menter BSL model. The increased width has resulted in a longer L_{iso}, as well as a nearly monotonic rise in wall pressure. Hence, three-dimensional effects from the corners and side walls clearly have a significant impact on the isolator flowfield structure. The flow structure for both the 1×2 and 1×4 isolators are shown in Figs. 14 and 15, respectively. While there are several notable differences in the flows, the primary reason for the more monotonic centerline pressure rise for the larger aspect ratio case is the fact that the shock separated zone did not immediately re-attach along the z=0 centerline. The additional viscous damping made available by the larger separation region enhances diffusion; allowing the discrete pressure jumps across each shock reflection to smooth out prior to reaching the isolator surface.

Another item that deserves attention is the peculiar observation noted with the Menter SST and Wilcox 2006 models. Both of these models have built-in stress limiters that are designed to be more prone to separate when in the presence of an adverse pressure gradient. The Menter SST surface pressure values showed the expected trend of earlier boundary layer separation relative to the BSL version of the model. In fact, the SST model predicted the shock train to initiate 2 to 3 duct heights further upstream than the measurements indicate. Menter calibrated the SST model for transonic flows, and experience has shown [11] that it tends to over-predict the extent of separation for higher Mach number conditions. Hence, the over-prediction of

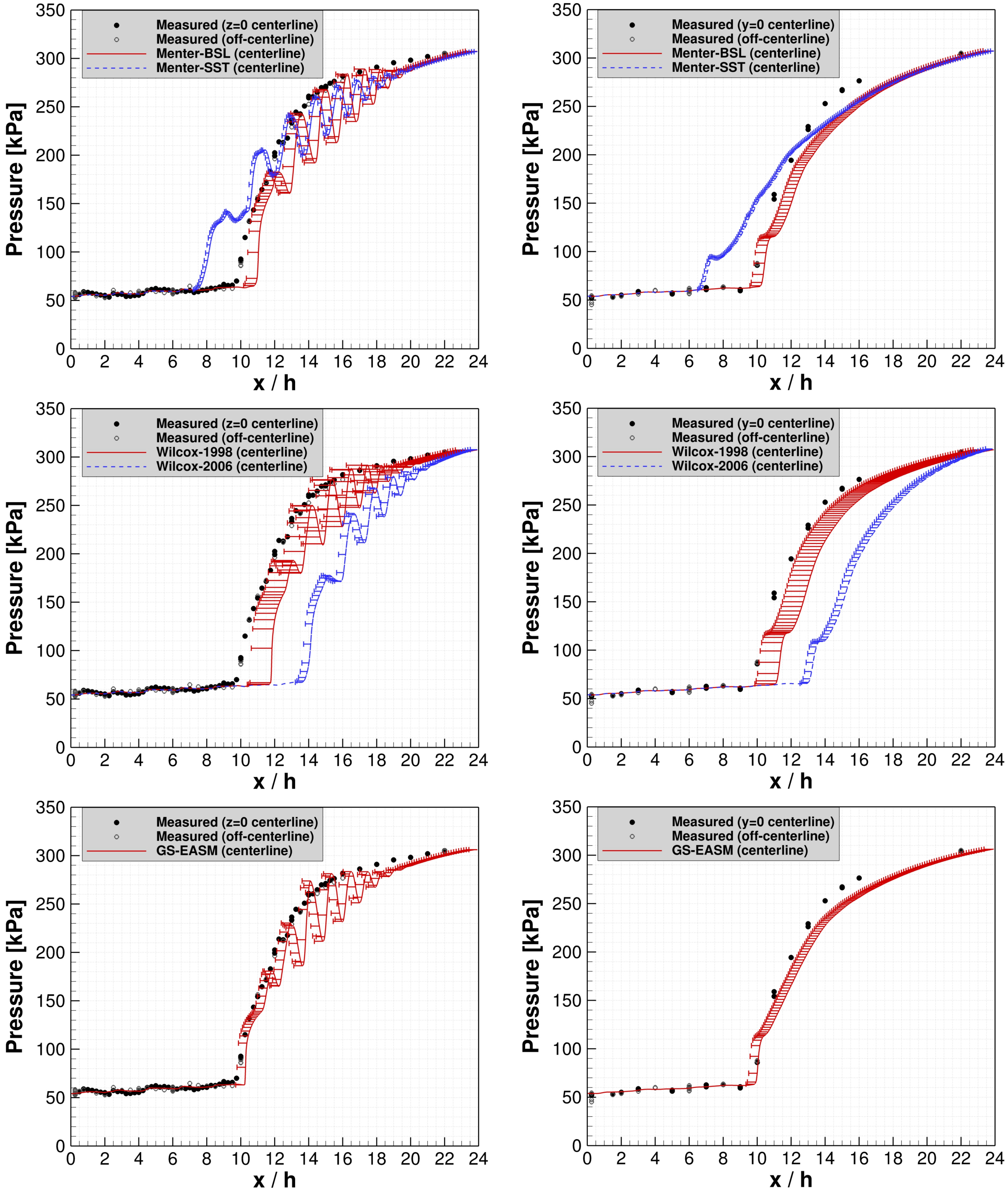

Figure 12: Comparison of measured wall pressure with computed results (medium grid) obtained for each turbulence model: top and bottom walls (left), side walls (right)

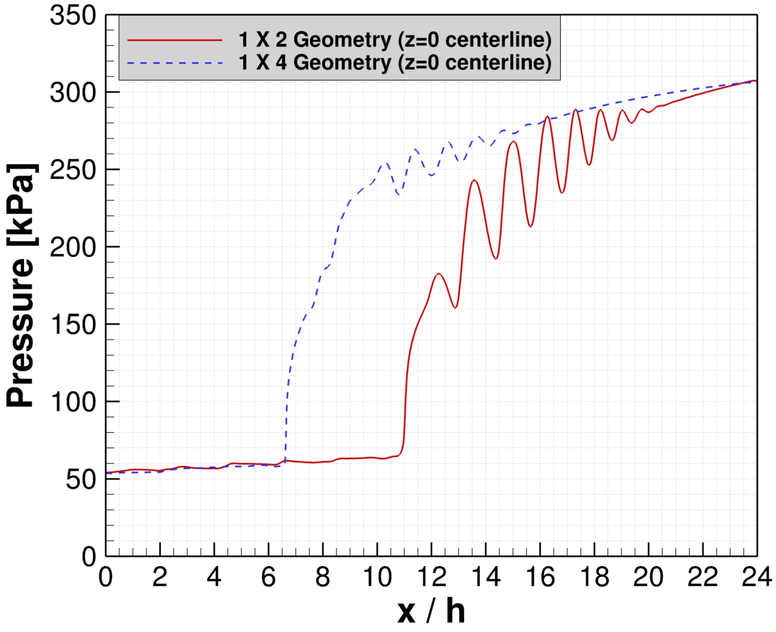

Figure 13: Comparison of spanwise centerline (z=0) surface pressure for the (1 × 2) and (1 × 4) geometries

L_{iso} was to some extent expected for this application. The Wilcox 2006 model, on the other hand, appears to have discouraged flow separation as compared with the other models considered (even those without a stress limiter). This result was not anticipated. Upon comparing this model to the Menter SST formulation, one finds that there are two fundamental functional differences other than the values specified for the constants. The first difference is the scalar parameter that controls the activation of the stress limiter. The Menter SST formulation uses the magnitude of the vorticity vector, while the Wilcox 2006 formulation uses the magnitude of the strain rate tensor. The second difference involves the turbulent diffusion terms in the transport equations for the turbulence kinetic energy and specific dissipation rate. The Wilcox 2006 model uses the non-limited eddy viscosity for these terms, while the Menter SST model uses the stress-limited eddy viscosity consistently for both the Navier-Stokes and turbulence transport equations.

A variant of the Wilcox 2006 model that uses the vorticity vector magnitude in lieu of the strain rate tensor magnitude is described in Ref. 11. This version of the model is touted as an acceptable substitute for the strain rate version by the model developer. However, it should be noted that practically all of the test cases used for the development of the Wilcox 2006 model are two-dimensional problems where there are far less terms involved that differentiate the strain rate tensor magnitude from the vorticity vector magnitude. An additional simulation was performed with this variant of the Wilcox 2006 model to examine the impact that this modification has on the stress limiter behavior. A comparison of the z=0 centerline pressure distributions obtained from each variant of the Wilcox 2006 model is shown in Fig. 16. The Wilcox 2006 model that uses the vorticity-based stress limiter shows flow separation at an earlier streamwise station. However, the shock train position is still further downstream than what was predicted by Wilcox 1998 model, which does not have a stress limiter. If one also alters the diffusion terms in the turbulent transport equations for k and ω to utilize the stress-limited eddy viscosity, one finds that this modified version of the Wilcox 2006 model predicts the same trend as the Menter SST model (see Fig. 16); in the sense that it predicts earlier separation than a similar model that does not invoke a stress limiter. The predicted shock system is further downstream than the Menter SST results because the Wilcox 2006 model uses a smaller stress limiter coefficient than the Menter SST model (to reduce the tendency to over-predict the extent of separation that plagues the SST model at higher Mach numbers). It should be emphasized that the intent of this exercise was to simply explain the differences in behavior between the Menter SST and Wilcox 2006 model and should not be interpreted as an endorsement for changing either of the models.

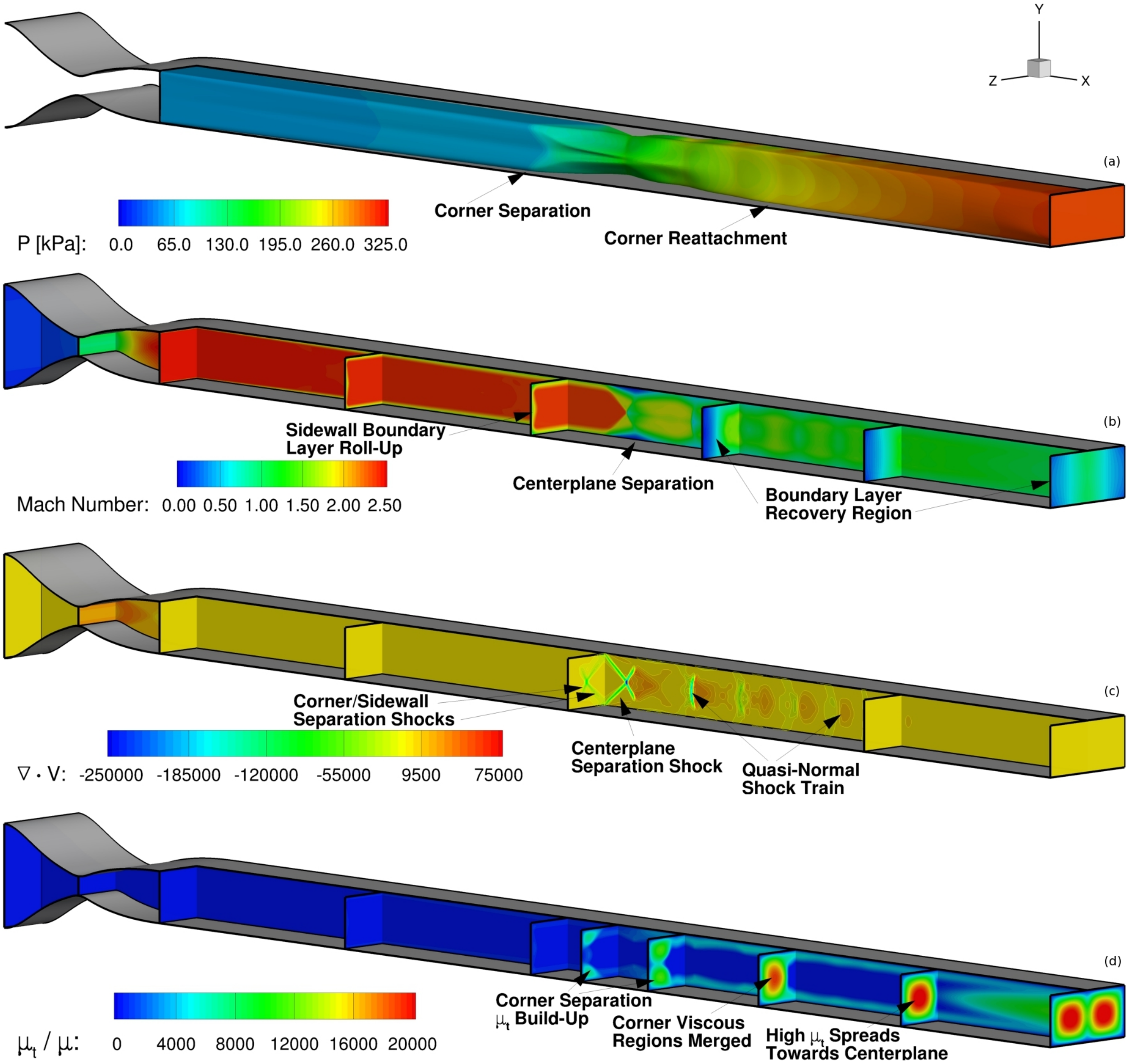

Figure 14: Isolator (1 × 2) flowfield characteristics: (a) total pressure iso-surface colored by static pressure contours, (b) Mach number contours (c) velocity divergence contours, (d) turbulent to molecular viscosity ratio contours

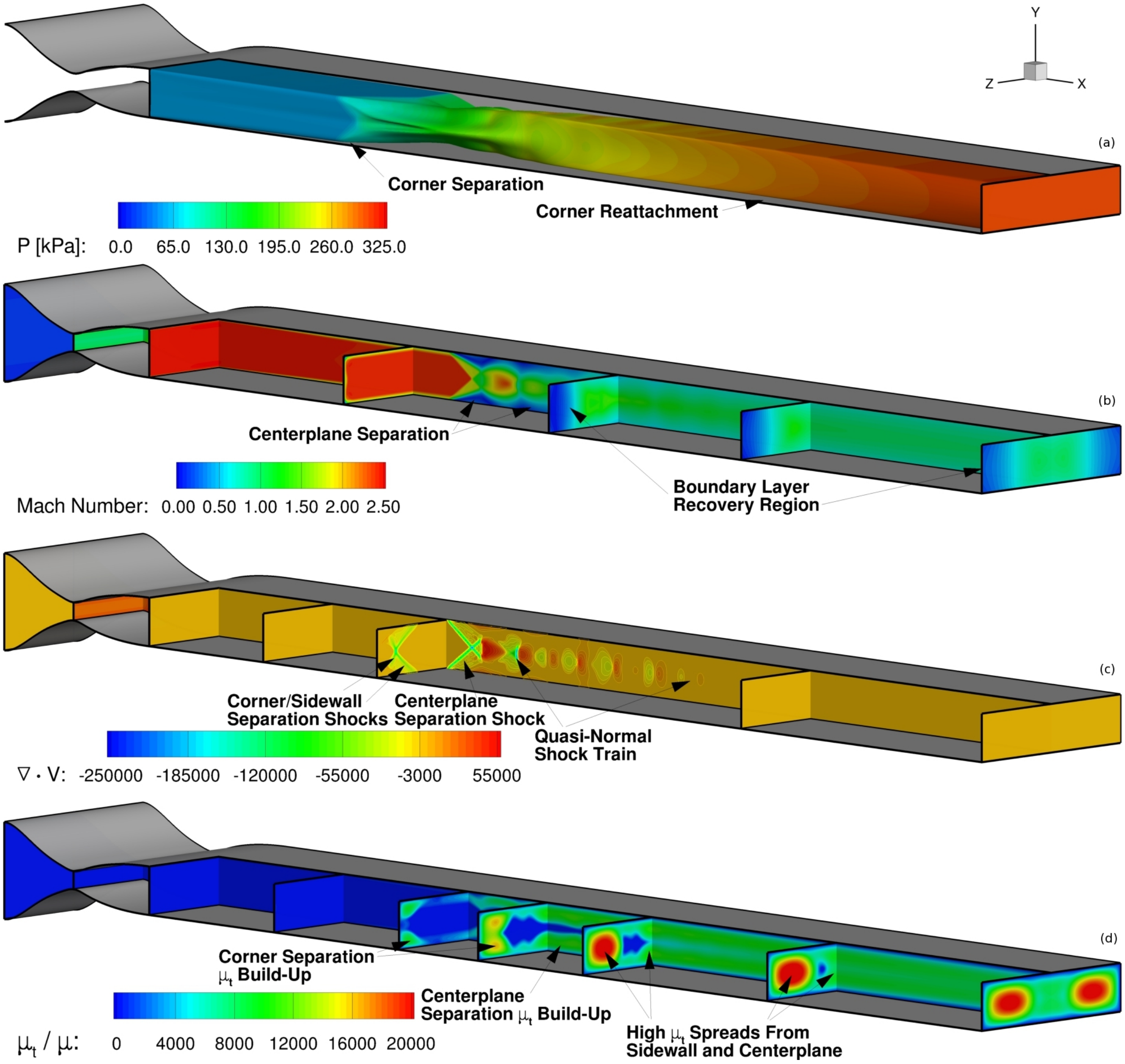

Figure 15: Isolator (1 × 4) flowfield characteristics: (a) total pressure iso-surface colored by static pressure contours, (b) Mach number contours (c) velocity divergence contours, (d) turbulent to molecular viscosity ratio contours

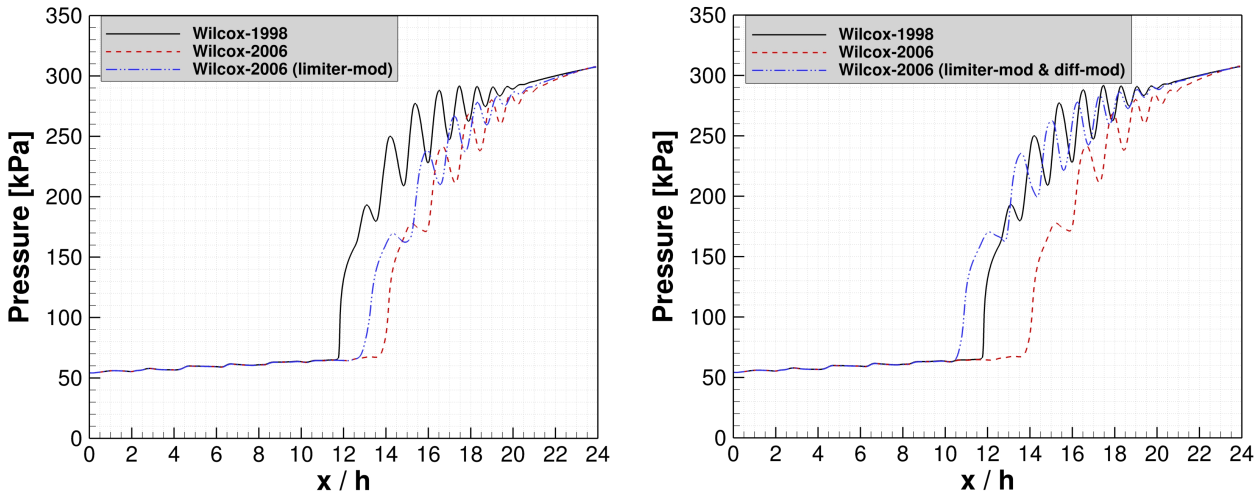

Figure 16: Effect of Wilcox 2006 modifications on the wall pressure (spanwise centerline); vorticity-based stress limiter (left), vorticity-based stress limiter and stress-limited diffusion in the turbulence transport equations (right)

SUMMARY AND FUTURE WORK

A research effort has been initiated to validate several turbulence closure models used for Reynolds-averaged simulations of scramjet isolator flows. This effort was crafted from its inception to couple both experimental and computational research teams to maximize the effectiveness of the validation exercise. The turbulence models considered in this validation effort were the Menter BSL, Menter SST, Wilcox 1998, Wilcox 2006, and the Gatski-Speziale explicit algebraic Reynolds stress models. A procedure to quantify the numerical errors was developed to account for discretization errors in the validation process. This procedure utilized the grid convergence index defined by Roache as a bounding estimate for the numerical error. The validation data, which presently is limited to surface pressure measurements, was collected from a mechanically back-pressured constant area (1 × 2 inch) isolator model with an isolator entrance Mach number of 2.5. Of the turbulence models considered, the models that did not include an explicit stress limiter more closely matched the measured surface pressures. This observation is somewhat surprising in a general sense, since stress limiters have generally been developed to better predict separation for flows subjected to an adverse pressure gradient. All of the models considered also failed to properly predict the shape and extent of the separated flow region caused by the shock boundary layer interactions. This conclusion was drawn via indirect evidence by noting that the measured surface pressures increased monotonically through the shock train, while the CFD predictions did not. Finally, while each of the turbulence models failed to properly predict all of the flow structure details associated with this massively separated flow, the best performing models were able to predict the shock train length to within 1 isolator duct height. The prediction of this metric is critically important, since it drives the overall length (and weight) of the isolator section.

The validation of closure models is a process, and this effort has documented only the initial stages of this process. Future work will focus on quantifying the uncertainty of the experimental effort. This will not only include the measurement uncertainty, but also attempt to include the uncertainty that results from geometry imperfections and facility operations. These additional considerations will likely rely on both simulation and measured data. A more in-depth analysis of the turbulence models for this massively shock separated flow will also be performed. In particular, a detailed comparison of the turbulence energy budgets may shed some light on why the shock-separated corner and side wall portions of the flow displayed unchecked turbulence production, while other shock-separated regions did not. Finally, the models will be subjected to different facility stagnation conditions and back pressures for validation over more than just the target 80%

normal shock pressure condition, and to flesh out any Reynolds number effects.

ACKNOWLEDGMENTS

This effort was funded through the High-Speed Project of the Fundamental Aerodynamics Program and carried out at the Hypersonic Airbreathing Propulsion Branch at the NASA Langley Research Center. Computational resources for this work were provided by the NASA Langley Research Center and the NASA Advanced Supercomputing (NAS) Division.

REFERENCES

[1] Baurle, R. A. and Eklund, D. R., ***Analysis of Dual-Mode Hydrocarbon Scramjet Operation at Mach 4–6.5***, Journal of Propulsion and Power, 18(5):990–1002 (Sept.-Oct. 2002).

[2] Hagenmaier, M. A., Gruber, M. R., Hsu, K.-Y., and Eklund, D. R., ***A Study of Shock Trains in Constant Area and Divergent Rectangular Ducts***, 2002 JANNAF CS/APS/PSHS/MSS Joint Meeting (April 2002).

[3] Middleton, T. F., Balla, R. J., Baurle, R. A., Humphreys, W. M., and Wilson, L. G., ***The NASA Langley Isolator Dynamics Research Lab***, 2009 JANNAF CS/APS/PSHS Joint Meeting (Dec. 2009).

[4] VULCAN, ***http://vulcan-cfd.larc.nasa.gov/*** (Dec. 2012).

[5] Edwards, J. R., ***A Low Diffusion Flux-Splitting Scheme for Navier-Stokes Calculations***, Computers & Fluids, 26(6):635–659 (1997).

[6] Koren, B., ***A Robust Upwind Discretization Method for Advection, Diffusion and Source Terms***, in C. B. Vreugdenhil and B. Koren, editors, *Numerical Methods for Advection-Diffusion Problems*, pages 117–138, Braunschweig: Vieweg Verlag (1993).

[7] McBride, B. J. and Gordon, S., ***Computer Program for Calculation of Complex Chemical Equilibrium Composition and Applications, I. Analysis***, NASA Reference Publication 1311 (October 1994).

[8] McBride, B. J. and Gordon, S., ***Computer Program for Calculation of Complex Chemical Equilibrium Composition and Applications, II. Users Manual and Program Description***, NASA Reference Publication 1311 (June 1996).

[9] Menter, F. R., ***Zonal Two Equation k-ω Models for Aerodynamic Flows***, AIAA Paper 93-2906 (July 1993).

[10] Wilcox, D. C., ***Turbulence Modeling for CFD***, DCW Industries, Inc., 2nd edn. (1998).

[11] Wilcox, D. C., ***Turbulence Modeling for CFD***, DCW Industries, Inc., 3rd edn. (2006).

[12] Rumsey, C. L. and Gatski, T. B., ***Recent Turbulence Model Advances Applied to Multielement Airfoil Computations***, AIAA Journal, 38(5):904–910 (Sept.-Oct. 2001).

[13] Middleton, T. F., Balla, R. J., Baurle, R. A., and Wilson, L. G., ***Laser-Induced Thermal Acoustic Measurements in a Highly Back-Pressured Scramjet Isolator Model: A Research Plan***, 2008 JANNAF CS/APS/PSHS Joint Meeting (May 2008).

[14] Roache, P. J., ***Verification and Validation in Computational Science and Engineering***, Hermosa Publishers (1998).

[15] Sinha, K., Mahesh, K., and Candler, G. V., ***Modeling Shock Unsteadiness in Shock / Turbulence Interactions***, Physics of Fluids, 15(8):2290–2297 (2003).

[16] Sinha, K., Mahesh, K., and Candler, G. V., ***Modeling the Effect of Shock Unsteadiness in Shock-wave / Turbulent Boundary Layer Interactions***, AIAA Paper 2004-1129 (Jan. 2004).